Desalination and Water Treatment 322 (2025) 101152

Contents lists available at ScienceDirect

Desalination and Water Treatment

journal homepage: www.sciencedirect.com/journal/desalination-and-water-treatment/

Surface modification of sodium alginate-polyvinyl alcohol hydrogel beads using low-pressure cold plasma and application for methylene blue removal from water

Rizza Wijaya [a,b], Endar Hidayat [c], Seiichiro Yonemura [a,*], Sadaki Samitsu [c], Hiroyuki Harada [a], Yoshiharu Mitoma [a,d]

[a] Graduate School of Comprehensive Scientific Research, Program in Biological System Sciences, Prefectural University of Hiroshima, Shobara 727-0023, Japan
[b] Agricultural Technology Department, Study Program of Agricultural Engineering, Politeknik Negeri Jember, Jember 68101, Indonesia
[c] Data-driven Polymer Design Group, Research Center for Macromolecules and Biomaterials, National Institute for Materials Science, 1–2-1 Sengen, Tsukuba 305-0047, Japan
[d] Department of Integrated Science and Engineering for Sustainable Societies, Faculty of Science and Engineering, Chuo University, Tokyo 112-8551, Japan

ARTICLE INFO

Keywords:
Hydrogel beads
Low-pressure cold plasma (LPCP)
Surface modification
Adsorption
Methylene blue removal

ABSTRACT

This study investigates the adsorption efficiency of methylene blue (MB) from aqueous solutions using sodium alginate-polyvinyl alcohol (SA/PVA) hydrogel beads modified through low-pressure cold plasma (LPCP) treatment. The LPCP process significantly enhanced the surface properties of the hydrogel beads, improving their adsorption capacity from 27.48 % (untreated) to 53.03 % (P15 treatment) at pH 8.2. Plasma-treated beads exhibited substantially higher MB removal compared to untreated beads, with the highest adsorption capacity of 175.506 mg g^{-1} under the P15 treatment condition. Adsorption followed the Freundlich model with high correlation coefficients ($R^2 = 0.998$), suggesting multilayer adsorption on a heterogeneous surface. Adsorption kinetics adhered to a pseudo-second-order model ($R^2 > 0.98$), indicating chemisorption as the dominant mechanism. Thermodynamic analysis demonstrated spontaneous and endothermic adsorption ($\Delta G^\circ = -7.55$ kJ mol^{-1} at 333 K). Plasma-treated hydrogel beads showed excellent reusability, maintaining over 85 % adsorption efficiency after three cycles. These findings highlight the potential of LPCP-treated hydrogel beads as an effective and sustainable solution for MB removal in wastewater treatment applications.

1. Introduction

Industrial growth in almost all sectors, especially textile, and paper, where dyes are routinely added to most products, is one of the most common causes of water pollution when untreated waste flows into land resources or directly back into aquatic systems [1]. The presence of these dyes in water bodies leads to contamination, a decline in water quality, and the introduction of toxic substances, posing severe threats to aquatic organisms and human health. Addressing this environmental challenge is critical to safeguarding ecosystem integrity and public health [2]. Water pollution caused by the textile, pharmaceutical, and chemical industries is a significant environmental concern. Synthetic dyes stand out among these pollutants due to their efficiency and persistence. The global textile industry releases over 280,000 metric tons of synthetic dyes into aquatic environments annually [3]. Contamination with methylene blue (MB) in the field, particularly in large quantities or uncontrolled environments, will have broad effects such as aquatic toxicity, soil contamination, human health risks, and water contamination [4]. MB can impair the oxygen-carrying capacity of aquatic organisms, potentially causing suffocation. Additionally, MB can alter microbial populations in soil, disrupt nitrogen fixation, and negatively impact plant growth [5]. MB also can negatively influence human health; it is toxic in people and can lead to health problems in people. It may cause skin, eye, and respiratory irritations. Higher doses of it may result in side effects like nausea, vomiting, diarrhea, and, in extreme cases, hemolytic anemia [6]. MB presents a multidimensional ecological and human health challenge of scientific significance. At the molecular level, the MB defines toxicological traits like mutagenic potential, damage to cellular membranes, and disturbance of biochemical pathways. Experimental studies in the laboratory revealed that MB can

* Corresponding author.
E-mail address: yone@pu-hiroshima.ac.jp (S. Yonemura).

https://doi.org/10.1016/j.dwt.2025.101152
Received 27 January 2025; Received in revised form 19 March 2025; Accepted 27 March 2025
Available online 3 April 2025

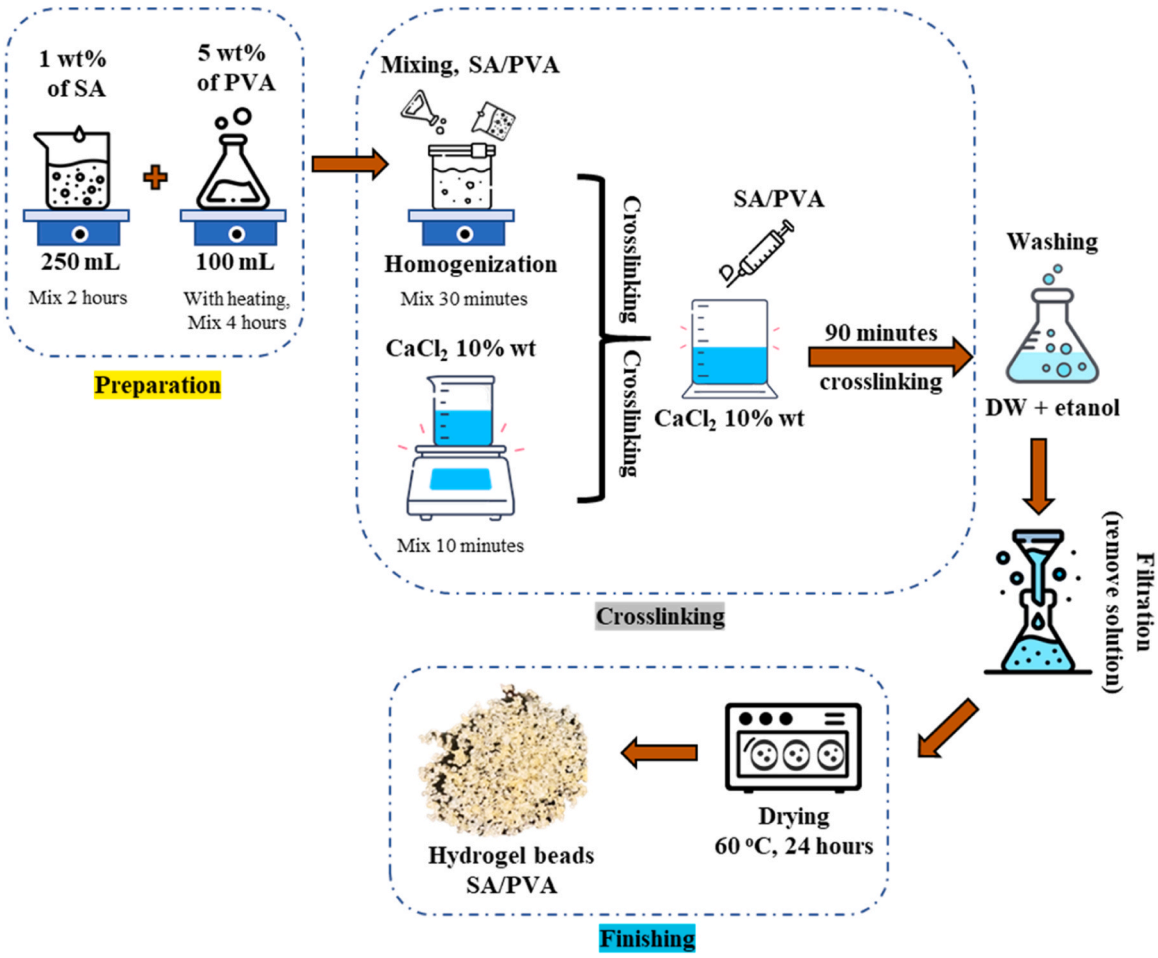

Fig. 1. Preparation of SA/PVA Hydrogel Beads.

induce oxidative stress and generate reactive oxygen species in biological systems, potentially leading to chromosomal aberrations [7].

Several approaches have been developed to reduce MB contamination, including cautious handling, proper storage in closed containers, and advanced waste management strategies. Various methods for removing MB have been examined, including adsorption, coagulation-flocculation, and membrane filtering [8]. The complex molecular structure of MB makes it quite resistant to conventional water treatment methods due to its chemical stability, strong intermolecular interactions, and persistent nature in aquatic environments [9]. Common physico-chemical treatment techniques, such as coagulation, flocculation, or adsorption, can remove only about 60–70 % of dyes, leaving substantial pollution in water systems [10].

Among these techniques, adsorption is a promising approach due to its cost-effectiveness, high efficiency, and environmental sustainability. Adsorption operates under mild conditions, requires minimal energy input, and can be applied to a wide range of adsorbents [11,12]. Several adsorbent materials have been reported for MB removal from water, including biochar [13,14], activated carbon [15,16], zeolites [17], clay minerals [18,19], metal-organic frameworks (MOFs) [20,21,22], and polymer-based adsorbents [23,24,25].

Hydrogel-based adsorbents have gained significant attention due to their high water retention, tunable porosity, and functional group availability, which enhance dye adsorption [26]. Among various hydrogel systems, sodium alginate (SA) and polyvinyl alcohol (PVA) are widely used due to their biocompatibility, non-toxicity, and ability to form stable hydrogel networks. SA, a natural polysaccharide, provides a biodegradable matrix with abundant carboxyl (-COOH) groups that facilitate MB binding. PVA enhances the hydrogels mechanical stability, elasticity, and reusability, making it an ideal component for adsorption applications [27].

Surface modifications are often required to improve the adsorption efficiency further. A promising technique for enhancing surface properties is cold plasma (CP) treatment, which induces physical and chemical modifications without altering the bulk properties of the material [28,29]. CP is an emerging surface modification technique that utilizes a partially ionized gas composed of energetic electrons, ions, free radicals, and reactive oxygen and nitrogen species (RONS) [30]. These reactive species interact with material surfaces, inducing both physical and chemical modifications without significantly altering the bulk properties [31]. One of the primary effects of CP treatment is the introduction of oxygen-containing functional groups, such as hydroxyl (-OH), carboxyl (-COOH), and carbonyl (C═O), which enhance surface hydrophilicity and create additional active adsorption sites [32]. These modifications improve electrostatic interactions between the adsorbent and target contaminants, such as methylene blue (MB), thereby enhancing adsorption performance. Furthermore, CP can alter surface morphology by introducing nano-scale roughness, increasing the available surface area for adsorption [33].

While CP has been widely applied for modifying various materials, its operational conditions vary depending on the plasma source, pressure, and gas composition. Atmospheric-pressure cold plasma (APCP) is commonly used due to its simplicity and scalability; however, it often suffers from non-uniform plasma distribution and limited control over reactive species, leading to inconsistent surface modifications [34]. In contrast, low-pressure cold plasma (LPCP) operates under vacuum conditions (typically below 100 Pa), allowing for better plasma uniformity, controlled reactive species generation, and deeper surface

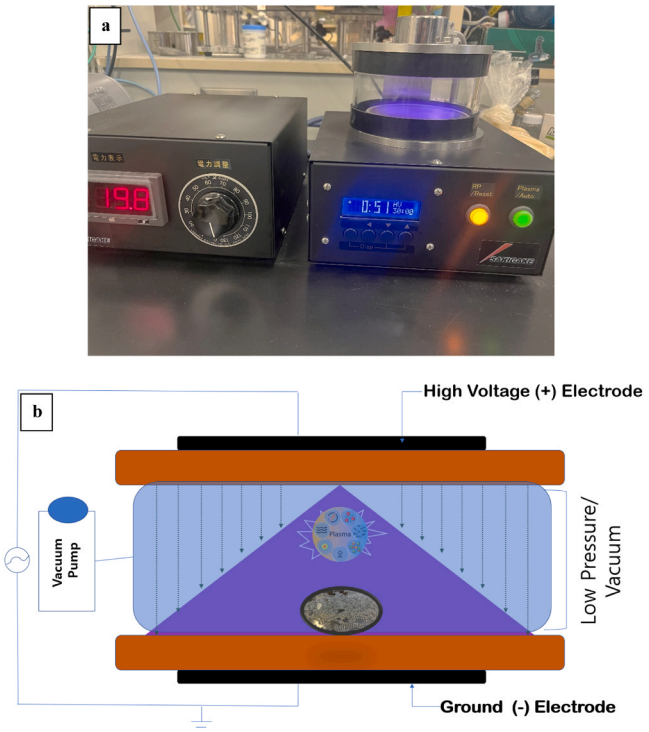

Fig. 2. (a) Vacuum plasma device (Sakage, YHS-R) and (b) schematic diagram of LPCP treatment for hydrogel beads.

penetration [35]. These advantages make LPCP particularly effective for modifying polymeric materials, including hydrogels.

Despite its potential, LPCP remains underexplored in hydrogel surface modification, particularly for water treatment applications. Most studies on CP-modified adsorbents have focused on carbonaceous materials such as activated carbon and biochar, while studies utilizing LPCP for hydrogel-based adsorbents remain limited [36]. In contrast, conventional chemical modification techniques, such as acid/base treatment, grafting polymerization, or functionalization with crosslinking agents, have been widely employed to introduce functional groups onto hydrogel surfaces [37,38]. However, these chemical methods often involve using toxic reagents, generating chemical waste, and may lead to unwanted structural degradation of the hydrogel matrix. In this study, we investigated the relationship between LPCP treatment conditions such as varying treatment times and the efficiency of MB removal from water. The findings of this study on the surface modification of SA/PVA hydrogel beads using LPCP aim to advance the development of more efficient water treatment technologies for removing MB from aqueous solutions.

2. Materials and method

2.1. Materials

Sodium alginate (SA) was purchased from Wako Chemicals, Tokyo, Japan. Calcium chloride ($CaCl_2$, ≥96.0 %), Hydrochloric acid (HCl, 36.0–38.0 %), methylene blue (MB), and sodium hydroxide (NaOH, ≥96.0 %) were purchased from Kanto Chemical Co. Inc., Japan. Polyvinyl alcohol (PVA, 98.0–99.0 %, hydrolyzed) was purchased from Thermo Scientific., Japan.

2.2. Preparation of SA/PVA hydrogel beads

The polymer solutions were prepared by dissolving 1 g of SA and 5 g of PVA in 100 mL of deionized water. PVA was initially solubilized in boiling water (approximately 100 °C) with continuous stirring until complete dissolution was achieved. Once the PVA was completely dissolved, the solution was allowed to cool slightly before the SA was added and mixed thoroughly to achieve a homogeneous solution. After dissolution, the reaction mixture was cooled to ambient temperature. The 1 wt% SA solution was mixed with the 5 wt% PVA solution in a flask to form hydrogel beads. The mixture was shaken for 30 minutes at room temperature (25°-30°C) using a water bath shaker to integrate and create the hydrogel precursor properly. The solution was then injected dropwise into a 10 wt% $CaCl_2$ aqueous solution previously prepared using a 10 mL syringe. The hydrogel beads were allowed to grow for 90 minutes to produce the final form before being rinsed with ethanol and distilled water and dried in an oven at 60°C for 24 hours (Fig. 1).

2.3. Plasma treatment

The samples were treated by a vacuum plasma machine (Sakigake, YHS-R) mounted with a vacuum pump (Ulvac Kiko inc, G-50DA) (Fig. 2a). The treatments were categorized as follows: NP (non-plasma) denotes untreated hydrogel beads, serving as the control; while P5, P10, and P15 were exposed to plasma treatment for 5 min, 10 min, and 15 min, respectively, under a vacuum chamber maintained at 0.1 bar with consistent power of 15 watts (Fig. 2b). After every treatment, the hydrogel beads were removed from the chamber and kept in airtight containers for further analysis.

2.4. Batch adsorption experiments

Batch adsorption experiments were conducted using a rotor (VMRC-5, As One) at an agitation speed of 100 rpm and a temperature of 30 °C. The experiments were conducted at three replicates to ensure the data's accuracy. 50 mL of a 10 mg L^{-1} dye solution and 0.01 g of adsorbent were placed into 100 mL glass flasks.

Isotherm analyses were conducted using a constant dosage of adsorbent 0.1 g in 200 mL of aqueous solution. Initial concentrations, such as 100, 200, 300, 400, 500, and 600 mg L^{-1}, were used at this stage [39]. While adsorption kinetics were performed using various contact durations of 5, 15, 30, 60, and 120 minutes. Adsorption thermodynamics were investigated at temperatures of 30, 40, 50, and 60 °C to assess the influence of temperature on the adsorption capacity. The MB dye removal percentage and adsorption capacity between the amounts adhere to the subsequent equations [40]:

$$\text{Dye removal } (\%) = \frac{(C_o - C_e)}{C_o} \times 100 \quad (1)$$

$$\text{qe} = \frac{(C_o - C_e)}{m} V \times 100 \quad (2)$$

Where q_e signifies the mass of the dye adsorbed by the adsorbent in 1 g of adsorbent material (mg g^{-1}), C_e is the level of concentration at equilibrium (mg L^{-1}), whereas C_o is the initial dye concentration, V is the total volume of solution composite (L), and m is the entire mass of the adsorbent (g).

2.5. Determination of carboxyl groups (-COOH)

The determination of carboxyl groups on hydrogel beads is accomplished through the poem's potentiometric titration method, which has been modified slightly [41]. Dry hydrogel beads were put into 2.5 mL NaCl solution (20 mM) and left for 30 minutes. After that, HCL was added until the pH of the solution reached 3.0. Then, the solution was added with NaOH immediately until the pH reached 11.0. -COOH can be analysed quantitatively by following the following method [42]:

$$-\text{COOH}(\text{mmolg}-1) = \frac{VNaOH \times MNaOH}{Wd} \quad (3)$$

Where, -COOH (mmol g^{-1}) means carboxyl content of the sample,

V_{NaOH}, the volume of NaOH added to the solution until it reaches a pH of 11.0, M_{NaOH} means NaOH molarity used, and W_d refers to the initial dry weight of the hydrogel beads used.

2.6. Swelling capacity

The study of swelling properties was conducted under room temperature for 24 hours on a batch shaker. The swelling capacity was investigated under different pH solutions of 4, 6, 8, and 10 to reflect different ionic conditions. These swelling properties could then be ascertained from the following equation [43]:

$$\text{Swelling}(\%) = \frac{W_1 - W_0}{W_0} \times 100 \quad (4)$$

Where W_1 and W_0 are the weight of swollen dried hydrogel beads and the dry weight of hydrogel beads, respectively.

2.7. Adsorption kinetics

Adsorption kinetics are crucial for evaluating the adsorption rate, as they directly affect the overall efficiency of the adsorption process. In the present study, we used pseudo-first-order and pseuso-second-order models. 0.01 g of the adsorbent was treated in a 20 mg L^{-1} of MB solution under ambient temperature on a batch shaker. MB solution were then collected at 5, 15, 30, 60, and 120 minutes and the solution concentrates were determined by UV-V values of the spectrophotometer. The linear adsorption capacity at that given time interval (q_t) was calculated using the Eqs. (5) and (6) [44]:

$$\text{qt} = \frac{(C_{0-C_t})V}{m} \quad (5)$$

$$\log(q_e - q_t) = \log q_e - K_1 t \quad (6)$$

$$\frac{t}{q_t} = \frac{1}{(K_2 \quad x \quad q_e)^2} + \frac{t}{q_e} \quad (7)$$

Where, q_t is adsorption capacity at time t (mg g^{-1}), C_0 is initial dye concentration (mg L^{-1}), C_t is dye concentration at time t (mg L^{-1}), V is volume of the solution (L), m is mass of the adsorbent (g), K_1 (min^{-1}) is the rate constant of the pseudo-first-order model, while t (min) represents time. K_2 represents the constant rate in pseudo-second-order models.

2.8. Adsorption isotherms

The adsorption isotherm tests involved equilibrating adsorbent with MB solutions of starting concentrations between 100 and 600 mg L^{-1} at room temperature. The remaining concentration of MB in the solution was quantified upon reaching equilibrium. The MB quantity adsorbed onto the hydrogel beads, q_e (mg g^{-1}), was determined in Eq. (7) [45]:

$$\text{qe} = \frac{\text{q}_{\text{max}}\text{K}_\text{L}\text{C}_\text{e}}{1 + \quad \text{K}_\text{L}\text{C}_\text{e}} \quad (8)$$

Where q_e is the equilibrium adsorption capacity (mg g^{-1}), q_{max} is the maximum adsorption capacity (mg g^{-1}), K_L is the Langmuir constant, which reflects the affinity between the adsorbate and adsorbent (L mg^{-1}), and Ce is the equilibrium concentration of MB in solution (mg L^{-1}). The values of K_L and q_{max} were determined through nonlinear regression. The Freundlich isotherm was determined by [46]:

$$qe = K_F C_e^{\,1/n} \quad (9)$$

Where, K_F (mg g^{-1}) is the adsorption equilibrium constant, signifying the adsorption capacity, and $1/n$ represents the adsorption intensity. The parameters K_F and $1/n$ were determined through the nonlinear fitting of the data.

The Temkin isotherm was expressed as:

$$q_e = \text{B } ln(K_T C_e) \quad (10)$$

where $\text{B} = \frac{R_T}{b}$ (J mol^{-1}) relates to the heat of adsorption, K_T (L mg^{-1}) is the equilibrium binding constant, is the universal gas constant (8.314 J mol^{-1} K^{-1}), and T is the absolute temperature (K). The Temkin model assumes that the adsorption heat decreases linearly with surface coverage.

The Redlich-Peterson isotherm was determined by:

$$\text{Qe} = \frac{K_R C_e}{1 + \beta C_e^{\gamma}} \quad (11)$$

Where K_R (L g^{-1}) is the Redlich-Peterson isotherm constant, β (L mg^{-1}) is a parameter related to adsorption strength, and γ is an exponent that ranges between 0 and 1, representing the degree of heterogeneity of the adsorption sites. The Redlich-Peterson model combines the characteristics of both Langmuir and Freundlich isotherms.

2.9. Adsorption thermodynamics

By determining the standard entropy (ΔS°), standard enthalpy (ΔH°), and standard Gibbs free energy (ΔG°), the thermodynamic properties of the MB dye adsorption process have been clarified. The equations defining their relationships are as follows [47]:

$$\text{Kc} = \quad \frac{q_e}{C_e} \quad (12)$$

$$\Delta G^\circ = \text{-}RT \ln K_c \quad (13)$$

$$\text{lnKc} = \frac{\Delta S^o}{R} - \quad \frac{\Delta H^o}{RT} \quad (14)$$

Where Kc is the equilibrium constant and R (8.314 J $mol^{-1}K^{-1}$) is the gas constant. q_e (mg g^{-1}) and C_e (mg L^{-1}) are the equilibrium concentration and adsorption amount, respectively. The slope and intercept of the plot between ln K_c and $1/T$ (45) were used to determine the ΔH° and ΔS°.

2.10. MB desorption and reusability

Following the MB adsorption process, the hydrogel beads were separated by centrifugation, dried, and subjected to desorption before reusing. The desorption process was optimized by evaluating the effects of different solvents (ethanol, distilled water, and various ethanol-distilled water ratios), desorption time (0.5–2 hours), and temperature variations (303–323 K) using a stepwise approach. Once the optimal desorption conditions were determined, the adsorbent was reused for adsorption under the optimized parameters, and the number of reuse cycles was recorded. The equations defining the desorption capacity are as follows [48]:

$$\text{Desorption capacity}(qde) \quad (\text{mg g} - 1) \quad = \quad \frac{VC_f}{m} \quad (15)$$

$$\text{Desorption efficiency } (\%) \quad = \quad \frac{C_f}{C_0}\text{x}100 \quad (16)$$

where V is the volume of the dye solution (L), m is the mass of the adsorbent used (mg),

CF is the final concentration of MB in the solvent (mg L^{-1}), and C_0 is the initial concentration of MB (mg L^{-1}).

2.11. Characterization

Surface images of the SA/PVA hydrogel beads was performed using Scanning electron microscope (SEM) linked with energy dispersive X-ray spectroscopy (EDS) Miniscope TM-4000 Plus II (Hitachi-Hitech,

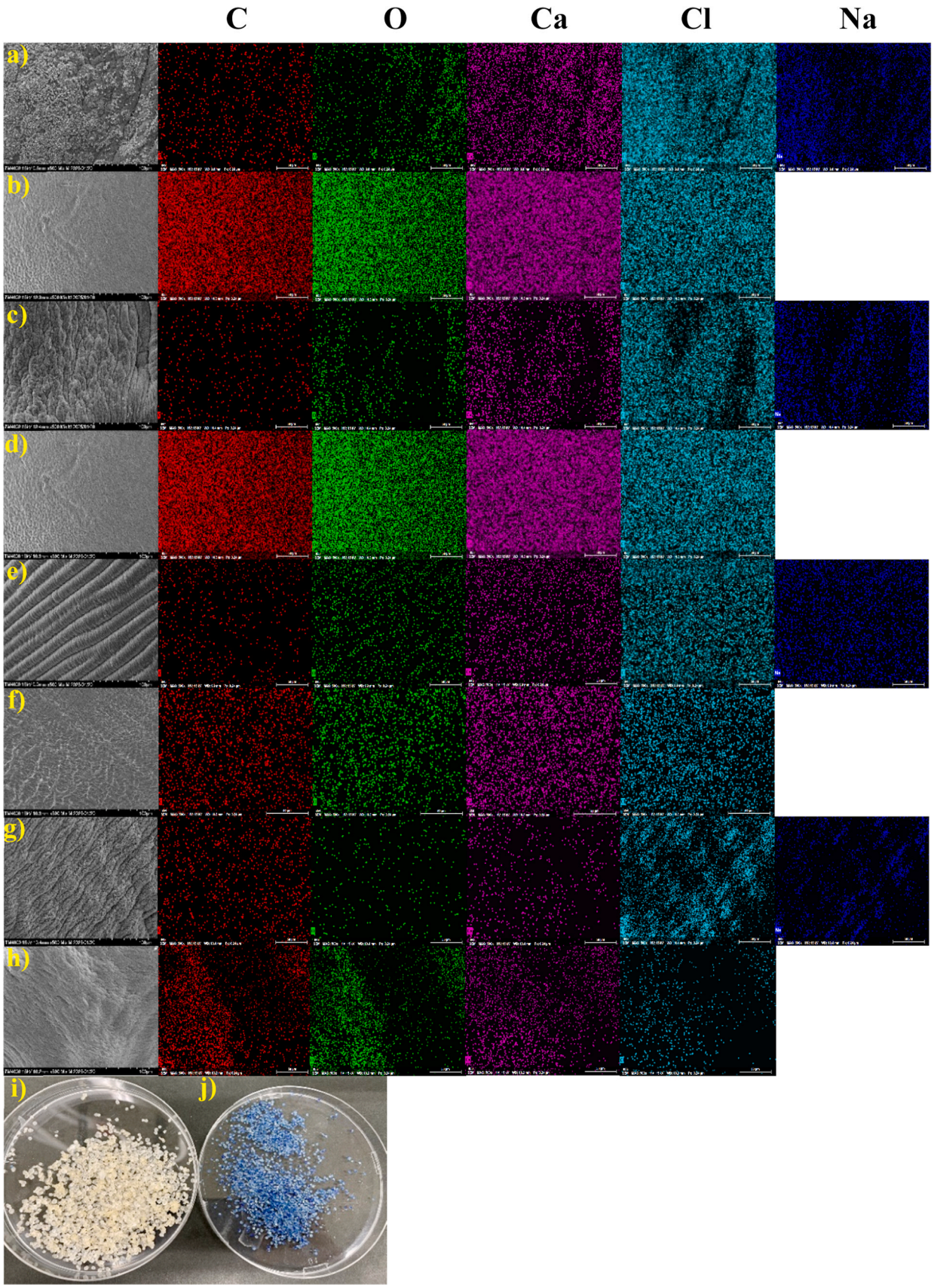

Fig. 3. SEM EDS of hydrogel beads (a) NP (before adsorption) (b) NP (after adsorption) (c) P5 (before adsorption) (d) P5 (after adsorption) (e) P10 (before adsorption) (f) P10 (after adsorption) (g) P15 (before adsorption) (h) P15 (after adsorption). Photograph of hydrogel beads (i) before adsorption (j) after adsorption.

Table 1
EDS data composition of hydrogel beads before and after adsorption.

Sample	Composition (Atom %)				
	C	O	Ca	Cl	Na
Before adsorption					
NP	40.84	21.59	5.03	18.38	14.15
P5	41.24	26.40	4.99	16.84	10.53
P10	37.77	35.29	5.09	15.10	6.75
P15	73.51	8.25	1.03	10.85	6.36
After adsorption					
NP	43.64	50.85	3.87	1.65	-
P5	46.58	48.96	3.31	1.15	-
P10	49.52	40.41	5.78	4.29	-
P15	46.84	48.70	3.63	0.83	-

Tokyo, Japan). ATR-FTIR assessed the adsorbent's functional groups from 500 to 4000 cm^{-1} (Thermo Scientific Nicolet iS10, Thermo Fisher Scientific Inc., Waltham, MA, USA). The residual concentration of MB before and after the experiment was evaluated using a UV-Vis spectrophotometer (JASCO V-530) at a wavelength of 664 nm.

3. Result and discussion

3.1. Characterization of hydrogel beads

The surface morphology of the hydrogel beads before and after the adsorption process was investigated using SEM imaging (Fig. 3). The results indicated that plasma treatment caused structural changes, such as ruptures or more open porosity in the hydrogel beads (P5, P10, and P15) (Fig. 3c, e, g), compared to the untreated sample (NP) (Fig. 3a), which are believed to enhance the adsorption process (Fig. 5a). Additionally, post-adsorption images of all samples (Fig. 3b, d, f, h) showed a more pliable surface, suggesting the uptake of MB onto the hydrogel bead surfaces. These findings suggest that LPCP treatment improved the surface functionality of the hydrogel beads, facilitating efficient MB adsorption from aqueous solutions[49]. The elemental composition of hydrogel beads was analyzed using SEM-EDS to evaluate the effects of plasma treatment and adsorption processes as shown in Table 1 in before adsorption, NP treatments showed a carbon (C) content of 40.84 % and oxygen (O) content of 21.89 %, reflecting the basic composition of the hydrogel beads matrix. The presence of calcium (Ca) and chlorine (Cl) due to sample preparation used $CaCl_2$ as crosslinking agent. Plasma-treated samples (P5, P10, P15) exhibited noticeable changes in composition, with an increase in O content (e.g., P5 and P10: 26.40 % and 35.29 %, respectively, and a reduction in Cl content. This result is consistent with a previous study [50,51], which showed that the elemental O content of the sample increased after plasma irradiation, possibly due to the introduction of O from the plasma source during the plasma crosslinking process. The prolonged plasma treatment in P15 resulted in the highest C content (73.51 %) and the lowest O content (8.25 %), suggesting enhanced surface carbonization or structural modifications caused by extended plasma exposure [52].

After adsorption, all samples exhibited significant increases in O content, indicating the incorporation of oxygenated species through adsorption [53]. For instance, the O content in NP increased from 21.59 % to 50.85 %, and in P15, it increased from 8.25 % to 48.70 %. Simultaneously, the Cl content decreased drastically across all samples (e.g., NP: 18.38–1.65 %, P5: 16.84–1.15 %, P10: 15.10–4.29 %, and P15: 10.85–0.83 %), suggesting ion exchange or replacement of Cl by other species during adsorption. Notably, C content also increased in all samples after adsorption, highlighting the deposition or interaction of organic molecules on the hydrogel surfaces [54]. P15 exhibited the most significant changes among the plasma treated samples, demonstrating its enhanced surface functionalization and adsorption capacity due to prolonged plasma exposure [55]. Moreover, the photograph of hydrogel beads before and after adsorption as shown in Fig. 3i-j. The color was changed to blue after adsorption, indicating the successful the adsorption process.

Table 2
Swelling properties and -COOH value of the hydrogel beads.

Treatment	Swelling (%)	-COOH (mmol g^{-1})
NP	14.14 ± 0.13^{a}	12.28 ± 0.02^{c}
P5	21.01 ± 0.07^{b}	6.78 ± 0.01^{b}
P10	24.78 ± 0.1^{c}	6.06 ± 0.02^{b}
P15	57.66 ± 0.12^{d}	5.08 ± 0.01^{a}

Mean values in the same column followed by different letters indicate significant differences ($P < 0.05$) according to Duncan's test.

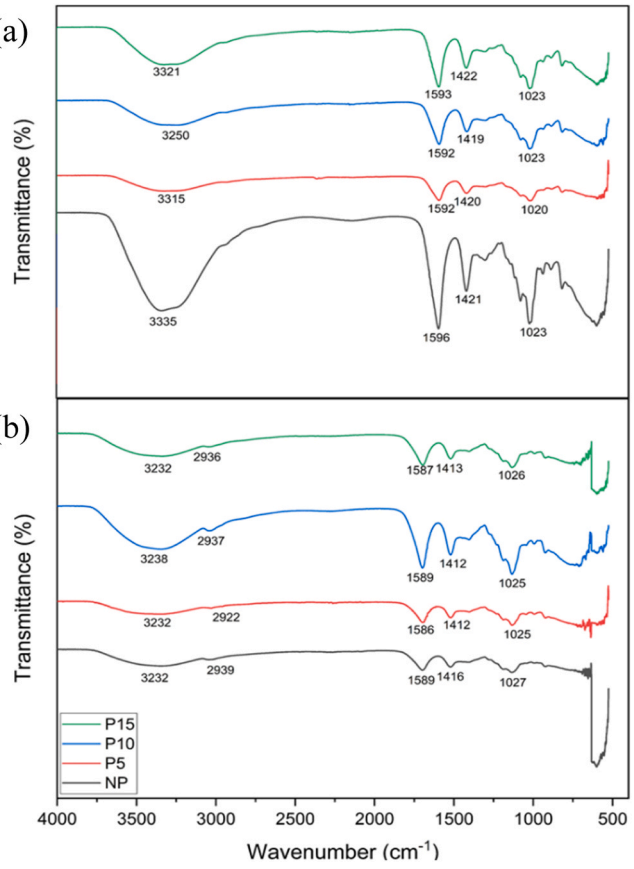

Fig. 4. FTIR spectra of hydrogel beads (a) before and (b) after adsorption of MB.

Table 2 demonstrates the effect of LPCP treatments on the physicochemical properties of the hydrogel beads. Statistical analyses show that LPCP treatments exhibited high significance for swelling properties ($P < 0.05$), in contrast with the COOH group ($P < 0.05$). It might have caused the decomposition of oxygen functional groups from the damaged hydrogel beads surface [56]. The results was similar to those reported previously [57], that used plasma treatment on fiber composites.

These results confirm the proposed mechanisms of LPCP surface modification, whereby high energy interacts and fuses with the hydrogel material, which leads to physical reconstruction (more surface area for interaction and increased surface roughness) and chemical functionalization (incorporation of polar hydroxyl, carboxyl, and carbonyl groups on the hydrogel surface) [58]. These will likely result in more enhanced hydrophilicity at the surface and greater density of active functional groups to facilitate better adsorption performance of SA/PVA hybrid hydrogel beads for water treatment, particularly the elimination of

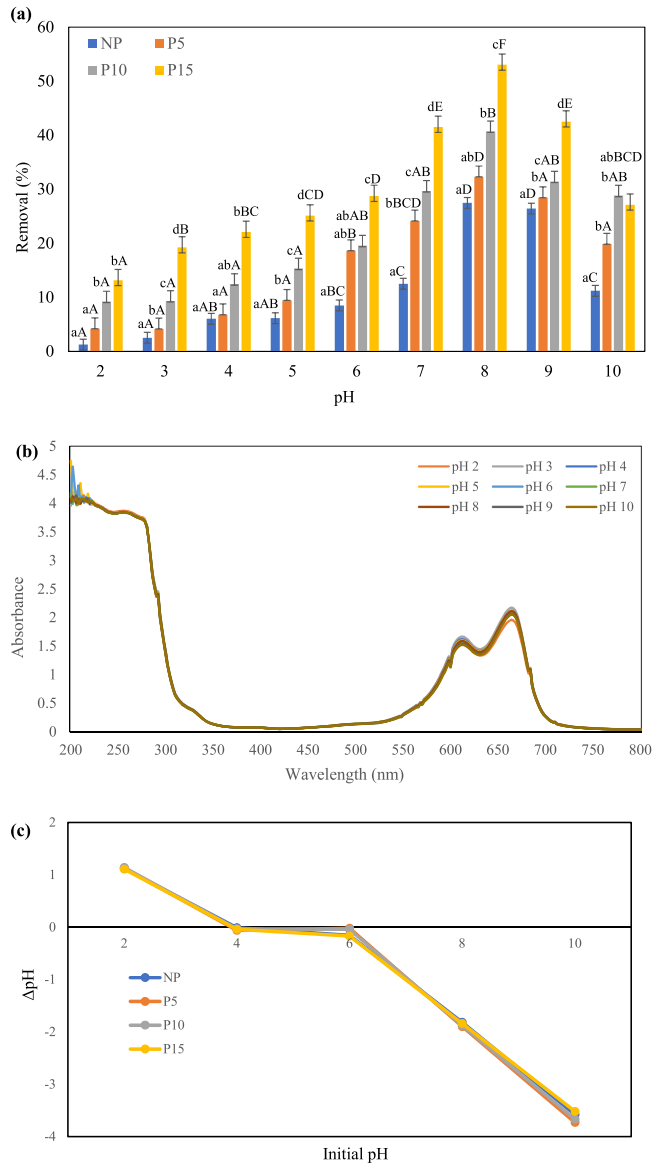

Fig. 5. (a) Effect of Initial pH on MB removal percentage. (b) UV-Vis Spectrum of MB Oligomer Formation (c) pH_{zpc} values of hydrogel beads. Different uppercase letters (A–C) on the bars within the same pH indicate significant differences. Different lowercase letters (a–b) on the bars within the same treatment indicate significant differences ($P < 0.05$).

cationic dyes, such as MB [59].

The FTIR spectra of the hydrogel beads as shown in Fig. 4. The data indicate changes in functional group peaks, namely in hydroxyl (O–H), carbonyl (C═O), and C–O–C bonds, which signify structural and bonding modifications caused by plasma exposure. The peak changes from 3335 cm^{-1} to 3321 cm^{-1} indicate O–H stretching, typically associated with hydroxyl groups [60]. Plasma treatment shifts these peaks to slightly lower wavenumbers, indicating a change in hydrogen bonding or interactions among hydroxyl groups. This transition suggests plasma treatment may modify the surface chemistry by strengthening hydrogen bonding or adding new surface hydroxyl groups [61]. The peaks around 1596–1592 cm^{-1} indicate C═O stretching in carboxylate groups, and exhibit minor shifts. The changes identified in this location indicate that plasma treatment may amplify these groups reactivity, thereby affecting the material's adsorption characteristics. Peaks between 1421 and 1304 cm^{-1} , associated with C–O stretching and O–H bending vibrations, exhibit variations, signifying alterations in the structure of carboxylate and hydroxyl groups. Plasma treatment likely influences the orientation or bonding of these groups, so reinforcing the notion that the surface chemistry is being altered. In the C–O–C stretching zone (1079–1023 cm^{-1}), crucial for the PVA and alginate backbone, variations in peak intensity and minor shifts in wavenumber are seen. This suggests that the plasma treatment causes rearrangements or cross-linking within the polymer foundation, altering the hydrogels structural characteristics [62]. The lower wavenumber range (below 1000 cm^{-1}) encompasses peaks associated with C–H bending and deformation modes, with intensity variations presumably indicating modifications in the hydrogel matrix due to plasma treatment [63]. The changes in peak positions and intensities indicate that plasma treatment continuously changes the hydrogel surfaces functional groups, with the modification amount increasing with longer exposure times. These changes improve the hydrophilicity and reactive sites on the hydrogel surface, potentially improving its adsorption capacity [64].

After adsorption, significant changes are observed in the plasma-treated and non-treated samples (Fig. 4b). The –OH stretching peaks shift to lower wavenumbers (e.g., 3232–2937 cm^{-1}) and decrease in intensity, indicating the involvement of hydroxyl groups in MB adsorption. The carboxylate peaks (1596–1587 cm^{-1} and 1421–1412 cm^{-1}) also shift and decrease, suggesting an interaction between the COO^- groups in the SA and the cationic MB dye. Furthermore, the peaks around 1025–1027 cm^{-1} show changes in transmittance, confirming that the adsorption process involves the C–O and C–O–C functional groups. Plasma-treated samples, particularly P15, display more pronounced spectral changes than NP, indicating enhanced interaction with MB due to the plasma-induced functional group activation. These results suggest that cold plasma treatment improves the hydrogel surface properties, enhancing its ability to adsorb MB efficiently [65].

3.2. *Initial pH effect*

The pH-dependent adsorption behavior of untreated and plasma-treated adsorbents was systematically investigated over a pH range of 2–10. The results (Fig. 5a) indicate that the adsorption efficiency increased with pH, reaching a maximum of 8.2 for all samples. The highest removal efficiency was observed for P15 (53.03 %), followed by P10 (40.72 %), P5 (32.29 %), and NP (27.48 %). This trend suggests that plasma treatment enhances the adsorption capacity of hydrogel beads by modifying surface functional groups, thereby increasing interaction sites for MB. At lower pH values (2.0–4.0), adsorption was significantly reduced, with removal efficiencies below 10 % for NP and P5, while P10 and P15 showed slightly higher efficiencies (up to 22.08 % for P15 at pH 4). The decrease in adsorption efficiency at acidic conditions is attributed to electrostatic repulsion between the cationic MB species and the protonated functional groups of the hydrogel beads [66].

The pKa of MB is approximately 3.8 [67], which influences its molecular speciation and adsorption behavior. At pH values below this range, MB predominantly exists in its monomeric cationic form (MB^+), leading to strong electrostatic repulsion from the positively charged hydrogel surface. Consequently, limited adsorption occurs due to reduced attractive interactions [68]. As pH increases beyond the pKa, MB deprotonates slightly, reducing electrostatic repulsion and facilitating stronger interaction with negatively charged hydrogel surfaces. This is particularly evident in the significant increase in removal efficiency at pH 6.0–8.0, where enhanced electrostatic attraction between MB and surface functional groups (e.g., carboxyl and hydroxyl groups) plays a dominant role [69]. The optimal adsorption observed at pH 8.2 suggests that MB is predominantly in its monomeric form at this pH, maximizing adsorption through electrostatic and hydrogen bonding interactions. At alkaline pH conditions (≥9.0), the adsorption efficiency decreased, likely due to the formation of MB oligomers. UV-Vis spectral analysis in the range of 200–800 nm confirmed this phenomenon

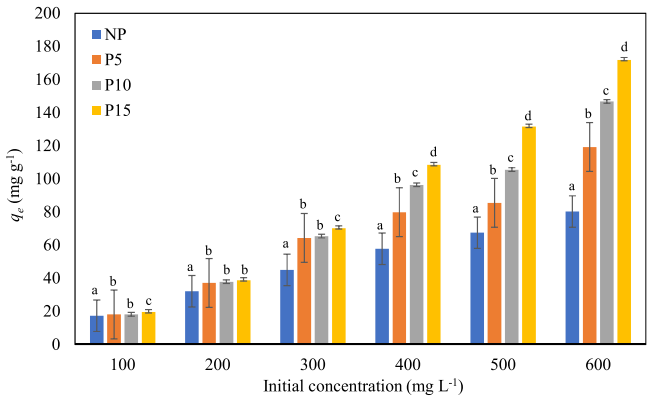

Fig. 6. Effect of initial concentration on MB removal percentage. Different lower-case letters indicate a significant difference in means ($P < 0.05$).

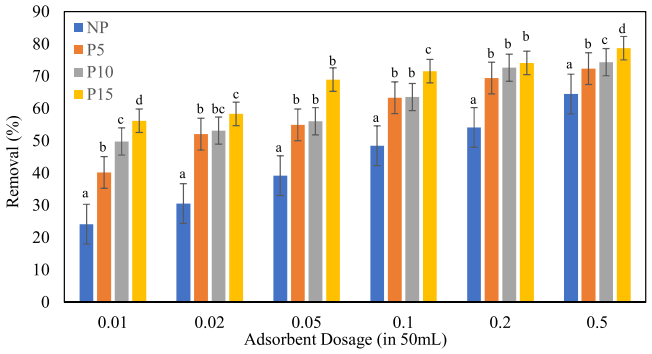

Fig. 7. Adsorbent dosage effects on the removal percentage of MB. Different lower-case letters indicate a significant difference in means ($P < 0.05$).

(Fig. 5b), as additional absorbance peaks at ~570 nm and 620–660 nm correspond to dimeric and aggregated MB species [70]. The formation of MB oligomers affects adsorption efficiency in two main ways: first, steric hindrance from larger molecular aggregates reduces their accessibility to adsorption sites, limiting interaction with the hydrogel surface. Second, the aggregation alters charge distribution, reducing electrostatic attraction between MB and the hydrogel, thereby decreasing adsorption efficiency at high pH values [71].

pH_{ZPC} analysis (Fig. 5c) further supports these observations, where a positive pH shift at low initial pH values (2.0–4.0) suggests significant uptake of H^+ ions by the hydrogel surface, whereas a negative pH shift at pH 8.0–10.0 indicates the release of H^+ ions into the solution. This amphoteric behavior is attributed to the presence of surface functional groups such as carboxyl (-COOH) and hydroxyl (-OH), which undergo protonation and deprotonation depending on the surrounding pH [72]. The consistent pH shift trends across plasma-treated and untreated samples suggest that plasma treatment enhances surface functionalization without significantly altering the isoelectric point of the hydrogel beads.

3.3. Impact of the initial MB concentration

Fig. 6 illustrates the effect of the initial methylene blue (MB) concentration on the adsorption capacity for different plasma treatments (NP, P5, P10, and P15). The adsorption capacity increased with increasing initial MB concentration, indicating that higher concentrations provide a stronger driving force for overcoming mass transfer resistance between the solution and the adsorbent surface. This trend reflects the enhanced availability of adsorption sites and improved surface interactions following plasma treatment. The plasma treated beads (P5, P10, and P15) consistently exhibited higher adsorption

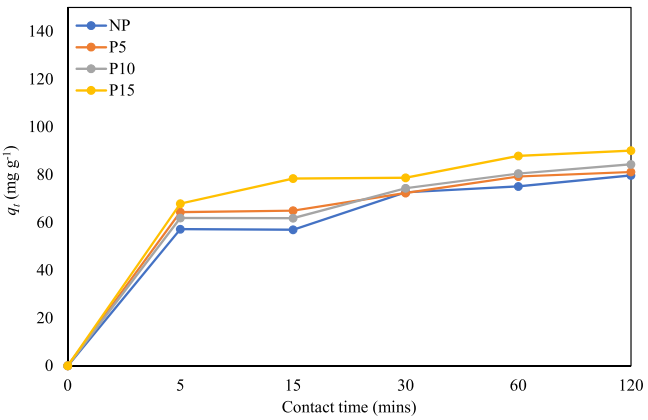

Fig. 8. Effect of contact time on removal percentage of MB.

capacity than the untreated beads (NP), confirming that plasma modification enhances surface functionality and active site availability. At the highest MB concentration (600 mg L^{-1}), the adsorption capacity reached 175.506 mg g^{-1} for P15, which was significantly higher than the untreated beads (NP) at 108.568 mg g^{-1}. Statistical analysis using different lowercase letters indicates significant differences in adsorption capacity among the treatments ($P < 0.05$). The increase in adsorption capacity with plasma treatment can be attributed to enhanced surface roughness, increased pore volume, and improved surface chemistry, which provide more active sites for MB adsorption [73]. The improved adsorption performance of the plasma-treated beads highlights plasma modifications effectiveness in enhancing the hydrogel beads adsorption capacity and surface interactions.

3.4. Effect of adsorbent dosage

Fig. 7 shows the effect of adsorbent dosage on MB removal efficiency. The results indicate that increasing the adsorbent dosage enhances removal efficiency, consistent with typical adsorption system behavior, where higher adsorbent concentrations provide more active sites, improving adsorption effectiveness [74]. At the lowest adsorbent dosage (0.01 mg in 50 mL solution), the P5 treatment exhibited the highest removal efficiency (~50 %), suggesting that plasma treatment enhances the surface characteristics of the beads, likely by increasing the surface area or introducing functional groups that promote interaction with MB molecules [75]. At the highest adsorbent dosage (0.5 mg), the P15 sample achieved the highest removal percentage (~80 %), indicating that increased surface modification leads to greater adsorption site availability until the beads reach their saturation point [76]. LPCP-treated samples (P5, P10, P15) exhibited higher removal efficiency across all adsorbent dosages compared to untreated samples (NP), confirming the positive effect of plasma treatment on adsorption performance.

Fig. 8 shows the effect of contact time on the removal efficiency of MB. The removal efficiency generally increases with contact time from 5 to 120 minutes, with the highest values observed at 120 minutes. This trend is consistent with typical adsorption behavior, where prolonged contact time enhances the interaction between the adsorbate (MB) and adsorbent (hydrogel beads), leading to greater removal efficiency [77].

The initial increase is most pronounced between 5 and 30 minutes, likely due to the high availability of adsorption sites at the beginning of the process. After 30 minutes, the increase becomes more gradual as the adsorption sites begin to reach saturation [78]. Plasma-treated beads (P5, P10, P15) exhibited higher removal efficiencies than untreated beads (NP) at all contact times, with the highest removal observed for the P15 sample, indicating that enhanced surface modification increases the adsorption capacity.

The adsorption kinetics of MB onto hydrogel beads were analyzed

Table 3
Kinetic parameters for the adsorption of MB onto hydrogel beads.

Kinetic models	Parameters	Treatment			
		NP	P5	P10	P15
Pseudo-first-order	qe (mg g^{-1})	2.158	2.567	2.056	2.855
	K_1 (g $mg^{-1}min^{-1}$)	0.0000125	0.0000142	0.0000133	0.0000583
	R^2	0.013	0.087	0.012	0.449
Pseudo-second-order	qe (mg g^{-1})	60.241	69.444	64.935	80.645
	K_2 (g $mg^{-1}min^{-1}$)	0.010	0.027	0.099	0.005
	R^2	0.996	0.998	0.995	0.987

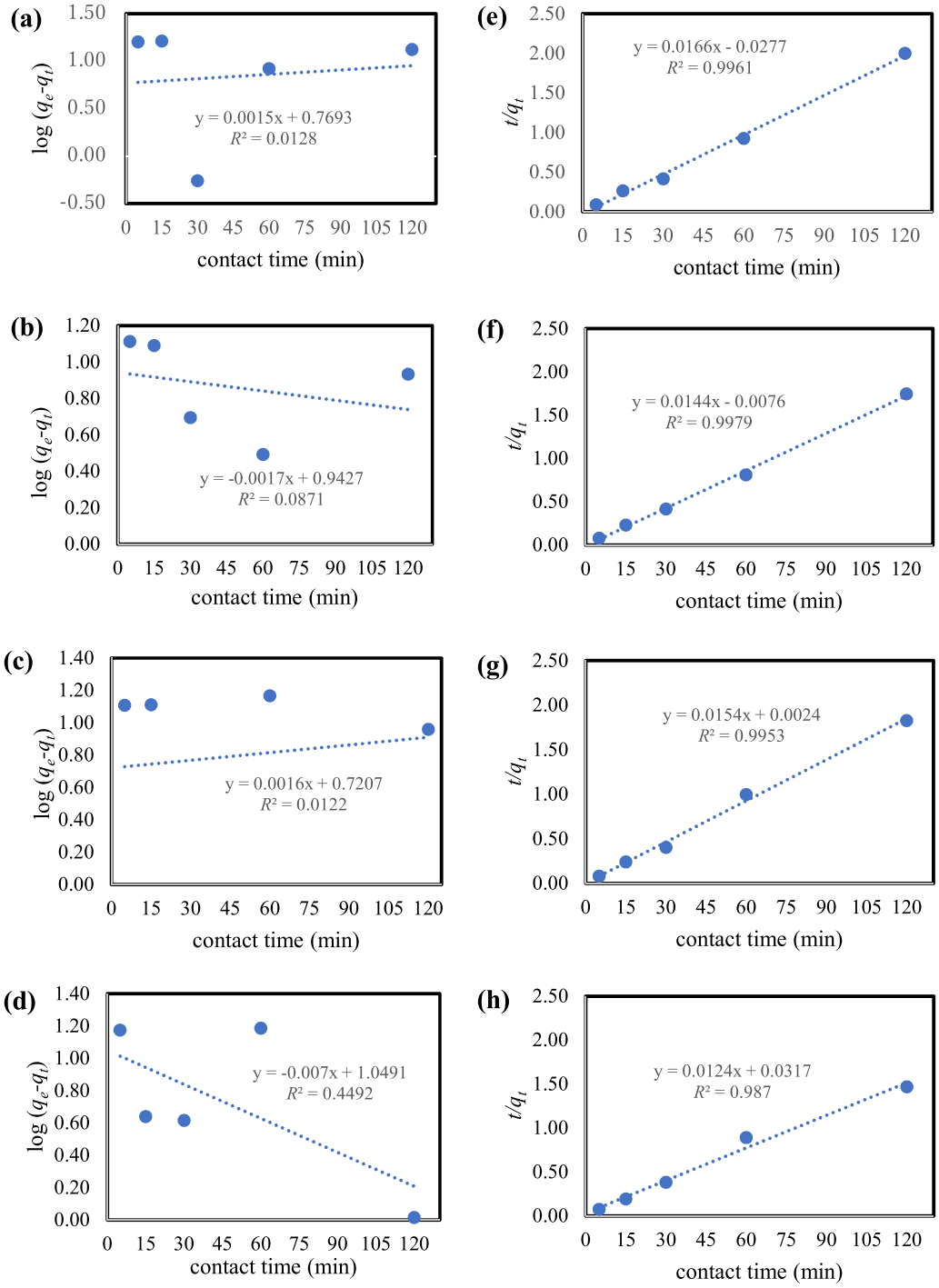

Fig. 9. Adsorption kinetics using (a)NP, (b) P5, (c) P10, (d) P15 pseudo-first-order and (e) NP, (f) P5, (g) P10, and (h) pseudo-second-order curves.

Table 4
Isotherm parameters for the adsorption of MB onto hydrogel beads.

Isotherm models	Parameters	Treatment			
		NP	P5	P10	P15
Langmuir	q_{max} (mg g^{-1})	108.568	112.315	147.900	175.506
	K_L (L mg^{-1})	1.224	2.178	2.440	5.364
	R_L	0.0081	0.0046	0.0041	0.0019
	R^2	0.954	0.932	0.903	0.858
Freundlich	K_F (g $mg^{-1}min^{-1}$)	27.673	143.193	141.595	530.264
	$1/n$	0.552	0.453	0.484	0.456
	R^2	0.998	0.933	0.904	0.961
Temkin	B	22.174	20.919	29.251	30.120
	K_T	0.133	0.305	0.231	0.674
	R^2	0.947	0.904	0.878	0.844
Redlich-peterson	β	0.0088	0.0229	0.0126	0.01298
	K_R	1.057	2.49	2.028	3.009
	R^2	0.977	0.839	0.842	0.893

Table 5
Thermodynamic adsorption of MB onto Hydrogel Beads.

	$\Delta G°$ (kJ mol^{-1})				$\Delta H°$ (kJ mol^{-1})	$\Delta S°$ (kJ $mol^{-1}K^{-1}$)
	303	313	323	333		
NP	−2.462	−2.643	−3.107	−7.553	37.210	128.767
P5	−2.660	−4.025	−4.387	−6.629	27.923	101.165
P10	−2.680	−2.913	−3.567	−5.923	22.751	82.902
P15	−3.782	−4.842	−6.155	−5.131	7.986	40.336

using pseudo-first-order and pseudo-second-order models. Table 3 demonstrates that the pseudo-second-order model provided a more accurate representation of the experimental data for all samples, shown by the higher R^2 values ranging from 0.987 to 0.998, compared to the pseudo-first-order model. This suggests chemisorption is probably the rate-limiting phase [79], as illustrated in Fig. 9.

The equilibrium adsorption capacity increased with the duration of plasma treatment, attaining its highest point of 80.645 mg g^{-1} at P15, with the lowest for the untreated sample (NP) at 60.241 mg g^{-1}. The improvement in adsorption capacity can be ascribed to enhanced surface characteristics, presumably resulting from improved functional group availability and modifications in surface area due to plasma exposure [80].

3.5. Adsorption isotherm analysis

Table 4 presents the linear regression coefficients (R^2) alongside key adsorption isotherm parameters for each treatment, highlighting the performance of the Langmuir and Freundlich models. The Freundlich model consistently exhibits superior R^2 values across all treatments (NP, P5, P10, and P15), with values ranging from 0.904 to 0.998, indicating a better fit for the experimental adsorption data. This suggests that the adsorption process may partially occur in a multilayer configuration under these conditions. The extended plasma treatment likely induces surface irregularities and heterogeneities, enhancing the complexity of the adsorption surface [81]. This is reflected in the significant increase in the Freundlich constant K_F, which rises from 27.673 (NP) to 530.264 (P15), indicating higher adsorption capacity with increased plasma treatment. Consequently, the Freundlich model, which accounts for non-uniform adsorption sites and multilayer adsorption, provides a more accurate description of the adsorption process [82].(Table 5)

The Langmuir model shows a progressive increase in maximum adsorption capacity (q_{max}) from 108.568 mg g^{-1} (NP) to 175.506 mg g^{-1} (P15), reflecting enhanced monolayer adsorption capacity with plasma treatment. The increase in q_{max} suggests that plasma treatment enhances the availability of active adsorption sites, possibly through surface activation or modification. However, the lower Langmuir regression coefficients (R^2) compared to the Freundlich model suggest that a heterogeneous surface model better represents the adsorption process rather than a uniform monolayer (Fig. 10).

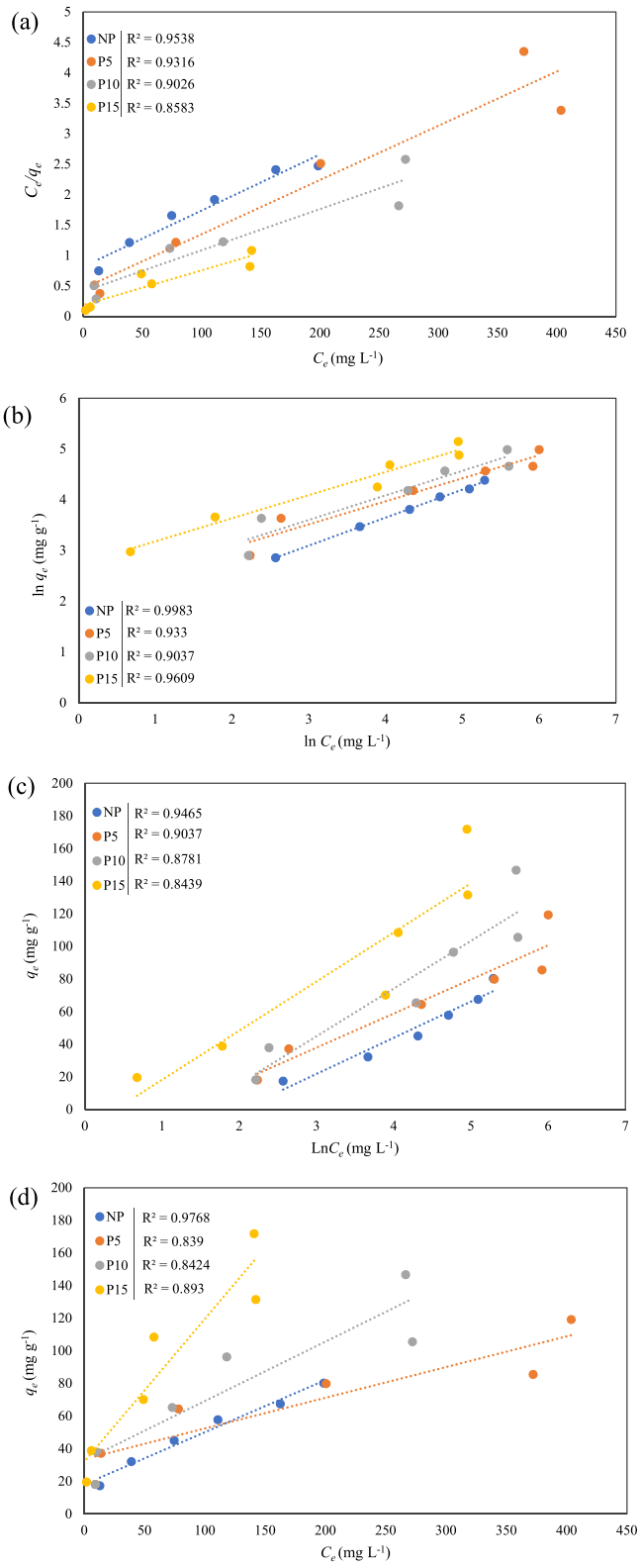

Fig. 10. Adsorption isotherm models of Langmuir (a), Freundlich (b), Temkin (c), and Redlich-peterson (d) for MB adsorption onto hydrogel beads.

Furthermore, the Temkin and Redlich–Peterson models were also

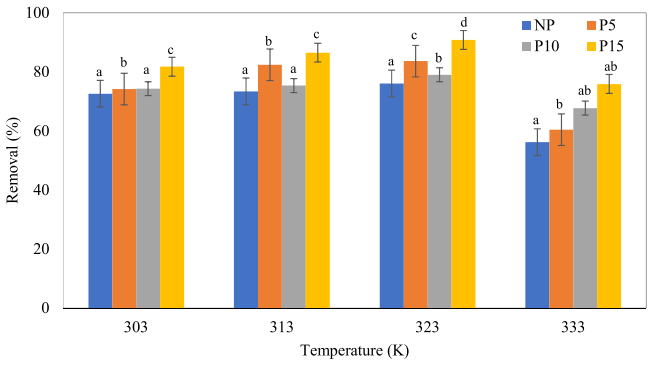

Fig. 11. Removal percentage of MB on different temperature. Different lowercase letters indicate a significant difference in means ($P < 0.05$).

evaluated to gain deeper insights into the adsorption mechanism [83]. The Temkin model considers the effect of indirect adsorbate–adsorbent interactions, while the Redlich–Peterson model combines features of the Langmuir and Freundlich models, capturing monolayer and multilayer adsorption characteristics. The Temkin constan and Redlich–Peterson constant

K_R increased with plasma treatment, supporting the hypothesis that surface heterogeneity and the number of available binding sites increased after plasma exposure. These findings align with the adsorption dynamics physical nature, emphasizing the adsorbent surfaces heterogeneous and multi-layered characteristics, particularly following plasma treatment [84]. Enhanced surface roughness and active site availability following plasma treatment likely contribute to the improved adsorption capacity and model fit observed in the Freundlich and Redlich–Peterson models.

3.6. Adsorption thermodynamics

Adsorption efficiency rises with temperature from 303 K to 323 K for most treatments, indicating improved adsorbate-adsorbent interaction at high temperatures (Fig. 11). A reduction in removal effectiveness is observed at 333 K, which may be attributed to the desorption effect or a decreased affinity of adsorbates at higher temperatures. For instance, the Gibbs free energy for the NP treatment decreases from -2.462 kJ mol^{-1} at 303 K to -7.553 kJ mol^{-1} at 333 K. This highlights the pronounced impact of elevated temperatures on adsorption efficiency, potentially due to weakened interactions between the adsorbent and adsorbate at higher thermal conditions [85].

This discovery aligns with the endothermic characteristics of adsorption, wherein increasing temperatures initially enhance diffusion and adsorption but may ultimately reduce surface adsorption forces [86, 87]. The cold plasma treatment enhances the materials adsorption characteristics with extended exposure times, such as P15, providing maximum removal effectiveness at all temperatures. This improvement may arise from augmented surface functionality such as carboxyl and hydroxyl groups or enhanced porosity achieved through plasma treatment, as indicated in prior research on adsorbent modifications [88].

The thermodynamic analysis shows that plasma treatment improves the adsorption characteristics of hydrogel beads. The negative Gibbs free energy (ΔG°) values for all samples signify spontaneous adsorption, with plasma-treated beads, particularly P15, exhibiting enhanced spontaneity, indicating that plasma treatment augments adsorption favorability (Table 4). The positive enthalpy (ΔH°) values for NP, P5, and P10 indicate an endothermic process wherein adsorption is facilitated by heat absorption. Nevertheless, ΔH° values diminish with increased LPCP treatment, indicating enhanced adsorption with less heat exchange, presumably resulting from plasma-induced structural alterations in the hydrogel [89,90]. Structurally, LPCP treatment likely increases surface smoothness and reduces irregularities, making the adsorption sites more uniform. It enhances surface polarity and functionality, facilitating stronger and more specific interactions with adsorbates. This improved organization reduces the randomness (entropy) of the adsorption process, as adsorbates bind more systematically to these optimized sites. LPCP treatment enhances the specific surface area and pore distribution of SA/PVA while increasing the density of functional groups, such as oxygen-containing groups. These structural changes promote a more predictable and ordered adsorption process, as evidenced by the reduction in ΔS° [91].

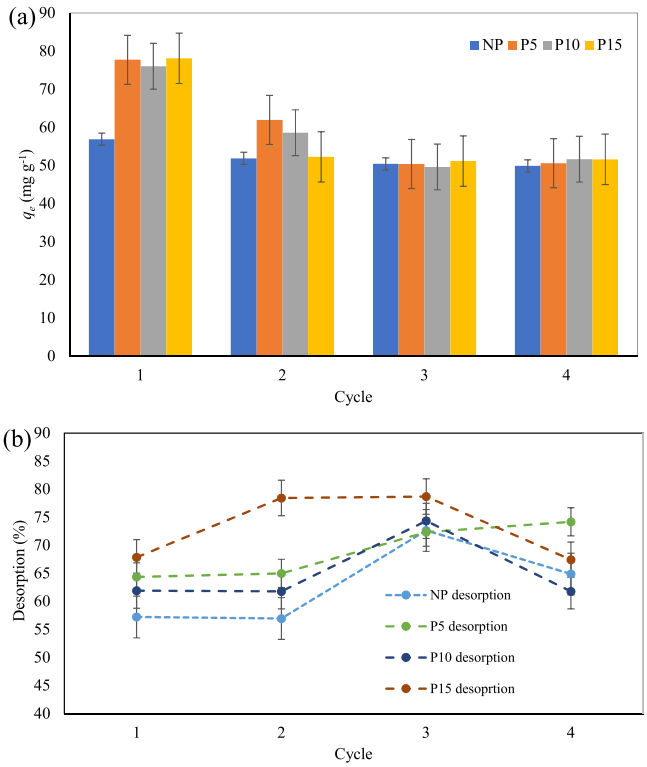

Fig. 12. (a) Reusability and (b) desorption efficiency of the hydrogel beads for MB removal from water.

Table 6
Comparison adsorbents for MB adsorption.

Adsorbent	q (mg g^{-1})	Reference
NP	108.57	This work
P5	112.32	This work
P10	147.9	This work
P15	175.51	This work
Au-NP loaded on activated carbon	40.65	[93]
Co_3O_4/SiO_2 nanocomposite	53.87	[46]
PAN-g-Alginate	3.51	[94]
H. cannabinus-g-PAA/PAAM	7	[95]
Carboxylate alginate	14	[96]
PVA/Bent hydrogel	27.90	[97]
Chitosan/organic rectorite composite	10.91	[98]
CS50SP50 composite adsorbent	40.98	[97]
Raw Ball clay	34.65	[99]

3.7. Reusability of SA/PVA hydrogel beads

The reusability data is shown in Fig. 12. Generally, plasma-treated hydrogel beads reveal high adsorption efficiency compared to the untreated sample. It might be indicated that even up to three cycles of the adsorption process, the hydrogel beads-treated plasma showed a good performance for MB removal from water. Furthermore, desorption data also showed a good performance for hydrogel beads treated plasma

compared to untreated sample. This is due to heightened surface roughness, more excellent hydrophilicity, and the incorporation of supplementary functional groups on the hydrogel surface. These alterations enhance the availability of active sites for dye molecule binding and improve dye removal efficiency [92].

3.8. Comparison of the maximum capacities with the previous adsorbents in literature

We compared our findings with previous research on the adsorption of MB from aqueous solutions using hydrogel beads, as summarized in Table 6. According to the literature, the P15 sample demonstrated superior performance. This suggests that the plasma exposure time plays a crucial role in enhancing the efficiency of MB removal from water.

4. Conclusion

Sodium alginate/polyvinyl alcohol (SA/PVA) hydrogel beads modified with low-pressure cold plasma (LPCP) were effectively utilized for the adsorption of methylene blue (MB) from aqueous solutions. The LPCP treatment significantly enhanced the beads' adsorption capacity, with the maximum adsorption capacity increasing from 108.568 mg g^{-1} (NP) to 175.506 mg g^{-1} (P15). Freundlich isotherm analysis showed that the adsorption process followed a multilayer mechanism, with the Freundlich constant (K_F) increasing from 27.673 (NP) to 530.264 (P15). Kinetic analysis confirmed that the adsorption followed a pseudo-second-order model (R^2>0.98), indicating chemisorption as the dominant mechanism. Thermodynamic analysis demonstrated that the process was spontaneous ($\Delta G^\circ = -7.55$ kJ mol^{-1} at 333 K) and endothermic, with increased adsorption at higher temperatures. After three cycles, plasma-treated hydrogel beads maintained over 85 % adsorption efficiency, highlighting their reusability and stability. These results underscore the potential of LPCP-treated hydrogel beads as an efficient and sustainable approach for wastewater treatment, warranting further research for broader environmental applications.

CRediT authorship contribution statement

Hidayat Endar: Writing – review & editing, Methodology, Formal analysis, Data curation, Conceptualization. **Wijaya Rizza:** Writing – original draft, Methodology, Investigation, Formal analysis, Data curation, Conceptualization. **Mitoma Yoshiharu:** Supervision. **Harada Hiroyuki:** Supervision. **Samitsu Sadaki:** Supervision, Data curation. **Yonemura Seiichiro:** Writing – review & editing, Supervision, Investigation, Formal analysis, Data curation, Conceptualization.

Declaration of Competing Interest

The authors declare that they have no known competing financial interests or personal relationships that could have appeared to influence the work reported in this paper.

Acknowledgments

The author (R.W) would like to sincerely thank the Ministry of Education, Culture, Sports, Science, and Technology (MEXT) Scholarship from the Government of Japan for supporting this research. The author also would like to thank Prof. Atsushi Hashimoto, Yukihiro Yamamoto, and Tomoyuki Yoshino for their invaluable guidance and suggestions during doctoral studies.

Data availability

Data will be made available on request.

References

[1] Kishor R, et al. Ecotoxicological and health concerns of persistent coloring pollutants of textile industry wastewater and treatment approaches for environmental safety. J Environ Chem Eng 2021;9(2):105012. https://doi.org/10.1016/j.jece.2020.105012.
[2] Islam T, Repon MR, Islam T, Sarwar Z, Rahman MM. Impact of textile dyes on health and ecosystem: a review of structure, causes, and potential solutions 2023; 30(4). https://doi.org/10.1007/s11356-022-24398-3.
[3] Jorge AMS, Athira KK, Alves MB, Gardas RL, Pereira JFB. Textile dyes effluents: a current scenario and the use of aqueous biphasic systems for the recovery of dyes. J Water Process Eng 2023;55:104125. https://doi.org/10.1016/j.jwpe.2023.104125.
[4] Al-Tohamy R, et al. A critical review on the treatment of dye-containing wastewater: ecotoxicological and health concerns of textile dyes and possible remediation approaches for environmental safety. Ecotoxicol Environ Saf 2022; 231:113160. https://doi.org/10.1016/j.ecoenv.2021.113160.
[5] Dimbo D, et al. Methylene blue adsorption from aqueous solution using activated carbon of Spathodea campanulata. Results Eng 2024;21:101910. https://doi.org/10.1016/j.rineng.2024.101910.
[6] Goluboff N, Wheaton R. Methylene blue induced cyanosis and acutehemolytic anemia complicating the treatment of methemoglobinemia. J Pedia 1961;58(1): 86–9. https://doi.org/10.1016/S0022-3476(61)80064-4.
[7] Oladoye PO, Ajiboye TO, Omotola EO, Oyewola OJ. Methylene blue dye: toxicity and potential elimination technology from wastewater. Results Eng 2022;16: 100678. https://doi.org/10.1016/j.rineng.2022.100678.
[8] Ihaddaden S, Aberkane D, Boukerroui A, Robert D. Removal of methylene blue (basic dye) by coagulation-flocculation with biomaterials (bentonite and Opuntia ficus indica). J Water Process Eng 2022;49:102952. https://doi.org/10.1016/j.jwpe.2022.102952.
[9] El Jery A, et al. Isotherms, kinetics and thermodynamic mechanism of methylene blue dye adsorption on synthesized activated carbon. Sci Rep 2024;14(1):1–12. https://doi.org/10.1038/s41598-023-50937-0.
[10] Mukhlish MZB, Khan MMR, Islam AR, Akanda ANMS. Removal of reactive dye from aqueous solution using coagulation-flocculation coupled with adsorption on papaya leaf. J Mech Eng Sci 2016;10(1):1884–94. https://doi.org/10.15282/jmes.10.1.2016.12.0180.
[11] Rathi BS, Kumar PS. Application of adsorption process for effective removal of emerging contaminants from water and wastewater. Environ Pollut 2021;280: 116995. https://doi.org/10.1016/j.envpol.2021.116995.
[12] Titchou FE, Zazou H, Afanga H, El Gaayda J, Akbour RA, Hamdani M. Removal of persistent organic pollutants (POPs) from water and wastewater by adsorption and electrocoagulation process. Groundw Sustain Dev 2021;13:100575. https://doi.org/10.1016/j.gsd.2021.100575.
[13] Ouedrhiri A, et al. Adsorption of the methylene blue dye in environmental water samples by biochar obtained from the valorization of argan shells. Phys Chem Res 2022;10(3):301–13. https://doi.org/10.22036/PCR.2021.303554.1968.
[14] Kujawska J, Wasag H. Biochar: a low-cost adsorbent of Methylene Blue from aqueous solutions. J Phys Conf Ser 2021;1736(1). https://doi.org/10.1088/1742-6596/1736/1/012002.
[15] Rattanet C, Knijnenburg JTN, Ngernyen Y. Kinetics and isotherm studies of methylene blue adsorption on activated carbon derived from chrysanthemum: solid waste of beverage industry. Nihon Enerugi Gakkaishi J Jpn Inst Energy 2022; 101(7):122–31. https://doi.org/10.3775/jie.101.122.
[16] El-Bery HM, Saleh M, El-Gendy RA, Saleh MR, Thabet SM. High adsorption capacity of phenol and methylene blue using activated carbon derived from lignocellulosic agriculture wastes. Sci Rep 2022;12(1):1–17. https://doi.org/10.1038/s41598-022-09475-4.
[17] Zhang L, Huang W, Dong X, Zhao Y, fang Li F, Cen Q hong. Improvement of zeolite adsorption ability for methylene blue by using electrospinning cellulose microfibers as template. Water Air Soil Pollut 2024;235(2):1–15. https://doi.org/10.1007/s11270-024-06899-8.
[18] "Adsorption of Methylene Blue Koji by Various IIMURA Clays and Zeolites National Institute of Agricultural Sciences"..
[19] M. El -Habacha, A. Dabagh, S. Lagdali, F. Sinan, M. Chiban, and M. Zerbet, "Methylene blue dye's adsorption on a natural clay surface from Southeast Morocco: modeling and experimental equilibrium studies," Environ. Sci. Pollut. Res., vol. Preprint, 2023.
[20] Wang S, et al. Enhanced methylene blue adsorption by cu-btc metal-organic frameworks with engineered particle size using surfactant modulators. Water 2022; 14(12). https://doi.org/10.3390/w14121864.
[21] Murtaza G, et al. Efficient adsorption of methylene blue using a hierarchically structured metal-organic framework derived from layered double hydroxide. ACS Omega 2024;9(14):16334–45. https://doi.org/10.1021/acsomega.3c10524.
[22] Li Y, Gao C, Jiao J, Cui J, Li Z, Song Q. Selective adsorption of metal-organic framework toward methylene blue: behavior and mechanism. ACS Omega 2021;6 (49):33961–8. https://doi.org/10.1021/acsomega.1c05299.
[23] Ma L, Liu W, Liu B, Tang YC. Removal of methylene blue by acrylic polymer adsorbents loaded with magnetic iron manganese oxides: synthesis, characterization, and adsorption mechanisms. Chemosphere 2024;346:140588. https://doi.org/10.1016/j.chemosphere.2023.140588.
[24] Zhu X, Zhang Z, Yan G. Methylene blue adsorption by novel magnetic chitosan nanoadsorbent. J Water Environ Technol 2016;14(2):96–105. https://doi.org/10.2965/jwet.15-072.

[25] Birniwa AH, et al. Adsorption behavior of methylene blue cationic dye in aqueous solution using polypyrrole-polyethylenimine nano-adsorbent. Polymers 2022;14 (16). https://doi.org/10.3390/polym14163362.
[26] Oyarce E, et al. Copolymeric hydrogels with high capacities of hydration and methylene blue adsorption in water. Polymers 2024;315(June). https://doi.org/10.1016/j.polymer.2024.127761.
[27] Wu Z, et al. Synthesis, characterization, and methylene blue adsorption of multiple-responsive hydrogels loaded with Huangshui polysaccharides, polyvinyl alcohol, and sodium carboxyl methyl cellulose. Int J Biol Macromol 2022;216: 157–71. https://doi.org/10.1016/j.ijbiomac.2022.06.178.
[28] Bormashenko E, Whyman G, Multanen V, Shulzinger E, Chaniel G. Physical mechanisms of interaction of cold plasma with polymer surfaces. J Colloid Interface Sci 2015;448:175–9. https://doi.org/10.1016/j.jcis.2015.02.025.
[29] Bertin M, Leitao EM, Bickerton S, Verbeek CJR. A review of polymer surface modification by cold plasmas toward bulk functionalization. Plasma Process Polym 2024;21(5). https://doi.org/10.1002/ppap.202300208.
[30] Thibodeaux N, Guerrero DE, Lopez JL, Bandelt MJ, Adams MP. Effect of cold plasma treatment of polymer fibers on the mechanical behavior of fiber-reinforced cementitious composites. Fibers 2021;9(10). https://doi.org/10.3390/fib9100062.
[31] Tabares FL, Junkar I. Cold plasma systems and their application in surface treatments for medicine. Molecules 2021;26(7). https://doi.org/10.3390/molecules26071903.
[32] Chytrosz-Wrobel P, Golda-Cepa M, Stodolak-Zych E, Rysz J, Kotarba A. Effect of oxygen plasma-treatment on surface functional groups, wettability, and nanotopography features of medically relevant polymers with various crystallinities. Appl Surf Sci Adv 2023;18(July):100497. https://doi.org/10.1016/j.apsadv.2023.100497.
[33] Oguzlu H, Baldelli A, Mohammadi X, Kong A, Bacca M, Pratap-Singh A. Cold plasma for the modification of the surface roughness of microparticles. ACS Omega 2024;9(33):35634–44. https://doi.org/10.1021/acsomega.4c03787.
[34] Yang X, Keener KM, Cheng JH. Enhancing the discharge uniformity of atmospheric pressure DBD cold plasma for food efficient microbial inactivation. J Food Eng 2025;388(October 2024):112389. https://doi.org/10.1016/j.jfoodeng.2024.112389.
[35] Ulbin-Figlewicz N, Brychcy E, Jarmoluk A. Effect of low-pressure cold plasma on surface microflora of meat and quality attributes. J Food Sci Technol 2015;52(2): 1228–32. https://doi.org/10.1007/s13197-013-1108-6.
[36] Kandel DR, et al. Cold plasma-assisted regeneration of biochar for dye adsorption. Chemosphere 2022;309(P1):136638. https://doi.org/10.1016/j.chemosphere.2022.136638.
[37] Kang YJ, et al. Acid treatment enhances performance of beads activated carbon for formaldehyde removal. Carbon Lett 2023;33(2):397–408. https://doi.org/10.1007/s42823-022-00428-5.
[38] Senkal BF, Bicak N. Grafting on crosslinked polymer beads by ATRP from polymer supported N-chlorosulfonamides. Eur Polym J 2003;39(2):327–31. https://doi.org/10.1016/S0014-3057(02)00224-0.
[39] Kittinaovarat S, Kansomwan P, Jiratumnukul N. Chitosan/modified montmorillonite beads and adsorption Reactive Red 120. Appl Clay Sci 2010;48 (1–2):87–91. https://doi.org/10.1016/j.clay.2009.12.017.
[40] Mousavi SA, Mahmoudi A, Amiri S, Darvishi P, Noori E. Methylene blue removal using grape leaves waste: optimization and modeling. Appl Water Sci 2022;12(5): 1–11. https://doi.org/10.1007/s13201-022-01648-w.
[41] Soto D, Urdaneta J, Pernia K. Characterization of native and modified starches by potentiometric titration. J Appl Chem 2014;(2014):1–9. https://doi.org/10.1155/2014/162480.
[42] Hidayat E, et al. Effects of sodium alginate-poly(acrylic acid) cross-linked hydrogel beads on soil conditioner in the absence and presence of phosphate and carbonate ions. Case Stud Chem Environ Eng 2024;9(December 2023):100642. https://doi.org/10.1016/j.cscee.2024.100642.
[43] Wang Q, Xie X, Zhang X, Zhang J, Wang A. Preparation and swelling properties of pH-sensitive composite hydrogel beads based on chitosan-g-poly (acrylic acid)/vermiculite and sodium alginate for diclofenac controlled release. Int J Biol Macromol 2010;46(3):356–62. https://doi.org/10.1016/j.ijbiomac.2010.01.009.
[44] Liu X, Zhang L. Removal of phosphate anions using the modified chitosan beads: Adsorption kinetic, isotherm and mechanism studies. Powder Technol 2015;277: 112–9. https://doi.org/10.1016/j.powtec.2015.02.055.
[45] Munagapati VS, Kim DS. Equilibrium isotherms, kinetics, and thermodynamics studies for congo red adsorption using calcium alginate beads impregnated with nano-goethite. Ecotoxicol Environ Saf 2017;141(March):226–34. https://doi.org/10.1016/j.ecoenv.2017.03.036.
[46] Abdel Ghafar HH, Ali GAM, Fouad OA, Makhlouf SA. Enhancement of adsorption efficiency of methylene blue on Co3O4/SiO2 nanocomposite. Desalin Water Treat 2015;53(11):2980–9. https://doi.org/10.1080/19443994.2013.871343.
[47] Xia Y qing, Guo T ying, Song M dao, Zhang B hua, Zhang B long. Adsorption dynamics and thermodynamics of Hb on the Hb-imprinted polymer beads. React Funct Polym 2008;68(1):63–9. https://doi.org/10.1016/j.reactfunctpolym.2007.10.018.
[48] Momina, Mohammad S, Suzylawati I. Study of the adsorption/desorption of MB dye solution using bentonite adsorbent coating. J Water Process Eng 2020;34 (January). https://doi.org/10.1016/j.jwpe.2020.101155.
[49] Iqbal M, Bhatti HN, Noreen S, Shukrullah S. Surface modification of heterostructured Bi8W4O24/ZrO2@GO composite via low-pressure cold plasma for boosting photocatalytic potential against Basic fuchsin and Bismarck brown Y dyes. Springe Berl Heidelb 2024;31(57). https://doi.org/10.1007/s11356-024-35541-7.
[50] Sasai Y, Komatsu A, ichi Kondo S, Yamauchi Y, Kuzuya M. Fabrication of hydrophilic polymer brushes on polystyrene substrate by plasma-based surface functionalization. J Photopolym Sci Technol 2012;25(4):551–4. https://doi.org/10.2494/photopolymer.25.551.
[51] Chen YM, et al. Bioinspired and self-restorable alginate-tyramine hydrogels with plasma reinforcement for arthritis treatment. Int J Biol Macromol 2023;250 (March):126105. https://doi.org/10.1016/j.ijbiomac.2023.126105.
[52] Rao J, Bao L, Wang B, Fan M, Feo L. Plasma surface modification and bonding enhancement for bamboo composites. Compos Part B Eng 2018;138(ember 2017): 157–67. https://doi.org/10.1016/j.compositesb.2017.11.025.
[53] Lee CS, Le Thanh T, Kim EJ, Gong J, Chang YY, Chang YS. Fabrication of novel oxygen-releasing alginate beads as an efficient oxygen carrier for the enhancement of aerobic bioremediation of 1,4-dioxane contaminated groundwater. Bioresour Technol 2014;171:59–65. https://doi.org/10.1016/j.biortech.2014.08.039.
[54] Yi B, et al. Surface hydrophobization of hydrogels via interface dynamics-induced network reconfiguration. Nat Commun 2024;15(1):1–13. https://doi.org/10.1038/s41467-023-44646-5.
[55] Ngo HT, Vu Thi Hong K, Nguyen TB. Surface modification by the DBD plasma to improve the flame-retardant treatment for dyed polyester fabric. Polymers 2021;13 (17). https://doi.org/10.3390/polym13173011.
[56] Sun R, et al. Construction of Fu brick tea polysaccharide-cold plasma modified alginate microgels for probiotic delivery: enhancing viability and colonization. Int J Biol Macromol 2024;268(P1):131899. https://doi.org/10.1016/j.ijbiomac.2024.131899.
[57] Cho BG, Hwang SH, Park M, Park JK, Park YBin, Chae HG. The effects of plasma surface treatment on the mechanical properties of polycarbonate/carbon nanotube/carbon fiber composites. Compos Part B Eng 2019;160(August 2018): 436–45. https://doi.org/10.1016/j.compositesb.2018.12.062.
[58] Mandolfino C. Polypropylene surface modification by low pressure plasma to increase adhesive bonding: effect of process parameters. Surf Coat Technol 2019; 366(February):331–7. https://doi.org/10.1016/j.surfcoat.2019.03.047.
[59] Gorbounov M, Halloran P, Masoudi Soltani S. Hydrophobic and hydrophilic functional groups and their impact on physical adsorption of CO2 in presence of H2O: a critical review. J CO2 Util 2024;86(August):102908. https://doi.org/10.1016/j.jcou.2024.102908.
[60] Zia F, Zia KM, Zuber M, Rehman S, Tabasum S, Sultana S. Synthesis and characterization of chitosan/curcumin blends based polyurethanes. Int J Biol Macromol 2016;92:1074–81. https://doi.org/10.1016/j.ijbiomac.2016.08.005.
[61] Bilek MM, McKenzie DR. Plasma modified surfaces for covalent immobilization of functional biomolecules in the absence of chemical linkers: towards better biosensors and a new generation of medical implants. Biophys Rev 2010;2(2): 55–65. https://doi.org/10.1007/s12551-010-0028-1.
[62] Mengjin WU, Lixia JIA, Suling LU, Zhigang QIN, Sainan WEI, Ruosi YAN. Interfacial performance of high-performance fiber-reinforced composites improved by cold plasma treatment: a review. Surf Interfaces 2021;24(February):101077. https://doi.org/10.1016/j.surfin.2021.101077.
[63] Sánchez-Soto M, Pagés P, Lacorte T, Briceño K, Carrasco F. Curing FTIR study and mechanical characterization of glass bead filled trifunctional epoxy composites. Compos Sci Technol 2007;67(9):1974–85. https://doi.org/10.1016/j.compscitech.2006.10.006.
[64] Duan S, et al. Highly enhanced adsorption performance of U(VI) by non-thermal plasma modified magnetic Fe3O4 nanoparticles. J Colloid Interface Sci 2018;513: 92–103. https://doi.org/10.1016/j.jcis.2017.11.008.
[65] Basak S, Annapure US. Rheological performance of film-forming solutions and barrier properties of films fabricated from cold plasma-treated high methoxyl apple pectin and crosslinked by Ca2+ : impact of plasma treatment voltage. Int J Biol Macromol 2023;227(December 2022):938–51. https://doi.org/10.1016/j.ijbiomac.2022.12.161.
[66] Lee H, Fiore S, Berruti F. Adsorption of methyl orange and methylene blue on activated biocarbon derived from birchwood pellets. Biomass– Bioenergy 2024;191 (October):107446. https://doi.org/10.1016/j.biombioe.2024.107446.
[67] Sousa HR, et al. Evaluation of methylene blue removal by plasma activated palygorskites. J Mater Res Technol 2019;8(6):5432–42. https://doi.org/10.1016/j.jmrt.2019.09.011.
[68] Luo T, Wang H, Chen L, Li J, Wu F, Zhou D. Visible light-driven oxidation of arsenite, sulfite and thiazine dyes: a new strategy for using waste to treat waste. J Clean Prod 2021;280:124374. https://doi.org/10.1016/j.jclepro.2020.124374.
[69] Al-Shaeli M, Benkhaya S, Al-Juboori RA, Koyuncu I, Vatanpour V. pH-responsive membranes: mechanisms, fabrications, and applications. Sci Total Environ 2024; 946(June):173865. https://doi.org/10.1016/j.scitotenv.2024.173865.
[70] Lewis GN, Goldschmid O, Magel TT, Bigeleisen J. Dimeric and other forms of methylene blue: absorption and fluorescence of the pure monomer. J Am Chem Soc 1943;65(6):1150–4. https://doi.org/10.1021/ja01246a037.
[71] Cavaliere P, et al. Binding of methylene blue to a surface cleft inhibits the oligomerization and fibrillization of prion protein. Biochim Biophys Acta - Mol Basis Dis 2013;1832(1):20–8. https://doi.org/10.1016/j.bbadis.2012.09.005.
[72] Björneholm O, Öhrwall G, De Brito AN, Ågren H, Carravetta V. Superficial tale of two functional groups: on the surface propensity of aqueous carboxylic acids, alkyl amines, and amino acids. Acc Chem Res 2022;55(23):3285–93. https://doi.org/10.1021/acs.accounts.2c00494.
[73] Alekseeva OV, Noskov AV, Titov VA, Nikitin D, Choukourov A, Agafonov AV. Adsorption performance of the polystyrene/montmorillonite composites: Effect of plasma treatment. Chem Eng Process - Process Intensif 2021;167(May):108505. https://doi.org/10.1016/j.cep.2021.108505.

[74] Rudi NN, et al. Evolution of adsorption process for manganese removal in water via agricultural waste adsorbents. Heliyon 2020;6(9):e05049. https://doi.org/10.1016/j.heliyon.2020.e05049.
[75] Demiral İ, Samdan C, Demiral H. Enrichment of the surface functional groups of activated carbon by modification method. Surf Interfaces 2021;22(September 2020). https://doi.org/10.1016/j.surfin.2020.100873.
[76] Wang T, Cao W, Wang Y, Qu C, Xu Y, Li H. Surface modification of quartz sand: a review of its progress and its effect on heavy metal adsorption. Ecotoxicol Environ Saf 2023;262(February):115179. https://doi.org/10.1016/j.ecoenv.2023.115179.
[77] İlktaç R, Bayir E. Magnetic hydrogel beads as a reusable adsorbent for highly efficient and rapid removal of aluminum: characterization, response surface methodology optimization, and evaluation of isotherms, kinetics, and thermodynamic studies. ACS Omega 2023;8(45):42440–56. https://doi.org/10.1021/acsomega.3c04984.
[78] Wu B, et al. Adsorption characteristics of used granular activated carbon regenerated by ultrasonic backwashing. Arab J Chem 2024;17(4). https://doi.org/10.1016/j.arabjc.2024.105704.
[79] Doğan M, Alkan M, Demirbaş Ö, Özdemir Y, Özmetin C. Adsorption kinetics of maxilon blue GRL onto sepiolite from aqueous solutions. Chem Eng J 2006;124(1–3):89–101. https://doi.org/10.1016/j.cej.2006.08.016.
[80] Kaseem M, Dikici B. Optimization of surface properties of plasma electrolytic oxidation coating by organic additives: a review. Coatings 2021;11(4):1–23. https://doi.org/10.3390/coatings11040374.
[81] Laureano-Anzaldo CM, González-López ME, Pérez-Fonseca AA, Cruz-Barba LE, Robledo-Ortíz JR. Plasma-enhanced modification of polysaccharides for wastewater treatment: a review. Carbohydr Polym 2021;252(July 2020). https://doi.org/10.1016/j.carbpol.2020.117195.
[82] López-Luna J, et al. Linear and nonlinear kinetic and isotherm adsorption models for arsenic removal by manganese ferrite nanoparticles. SN Appl Sci 2019;1(8):1–19. https://doi.org/10.1007/s42452-019-0977-3.
[83] de Oliveira C, et al. Evaluation of a graphitic porous carbon modified with iron oxides for atrazine environmental remediation in water by adsorption. Environ Res 2023;219(September 2022). https://doi.org/10.1016/j.envres.2022.115054.
[84] Babalar M, Siddiqua S, Sakr MA. A novel polymer coated magnetic activated biochar-zeolite composite for adsorption of polystyrene microplastics: synthesis, characterization, adsorption and regeneration performance. Sep Purif Technol 2024;331(September 2023):125582. https://doi.org/10.1016/j.seppur.2023.125582.
[85] Parida SK, Dash S, Patel S, Mishra BK. Adsorption of organic molecules on silica surface. Adv Colloid Interface Sci 2006;121(1–3):77–110. https://doi.org/10.1016/j.cis.2006.05.028.
[86] Bayuo J, Rwiza MJ, Choi JW, Mtei KM, Hosseini-Bandegharaei A, Sillanpää M. Adsorption and desorption processes of toxic heavy metals, regeneration and reusability of spent adsorbents: economic and environmental sustainability approach. Adv Colloid Interface Sci 2024;329(May). https://doi.org/10.1016/j.cis.2024.103196.
[87] Liu X, Sun J, Xu X, Alsaedi A, Hayat T, Li J. Adsorption and desorption of U(VI) on different-size graphene oxide. Chem Eng J 2019;360(March 2018):941–50. https://doi.org/10.1016/j.cej.2018.04.050.
[88] Williams J, Broughton W, Koukoulas T, Rahatekar SS. Plasma treatment as a method for functionalising and improving dispersion of carbon nanotubes in epoxy resins. J Mater Sci 2013;48(3):1005–13. https://doi.org/10.1007/s10853-012-6830-3.
[89] Chopra L, et al. Synthesis and characterizations of super adsorbent hydrogel based on biopolymer, Guar Gum-grafted-Poly (hydroxyethyl methacrylate) (Gg-g-Poly (HEMA)) for the removal of Bismarck brown Y dye from aqueous solution. Int J Biol Macromol 2024;256(P2):128518. https://doi.org/10.1016/j.ijbiomac.2023.128518.
[90] Zhao C, et al. Probing structure-antifouling activity relationships of polyacrylamides and polyacrylates. Biomaterials 2013;34(20):4714–24. https://doi.org/10.1016/j.biomaterials.2013.03.028.
[91] Zhou R, et al. Plasma-electrified up-carbonization for low-carbon clean energy. Carbon Energy 2023;5(1). https://doi.org/10.1002/cey2.260.
[92] Boycheva S, Szegedi Á, Lázár K, Popov C, Popova M. Advanced high-iron coal fly ash zeolites for low-carbon emission catalytic combustion of VOCs. Catal Today 2023;418(February 2022). https://doi.org/10.1016/j.cattod.2023.114109.
[93] Roosta M, Ghaedi M, Daneshfar A, Sahraei R, Asghari A. Optimization of the ultrasonic assisted removal of methylene blue by gold nanoparticles loaded on activated carbon using experimental design methodology. Ultrason Sonochem 2014;21(1):242–52. https://doi.org/10.1016/j.ultsonch.2013.05.014.
[94] Salisu A, Sanagi MM, Naim AA, Karim KJ. Removal of methylene blue dye from aqueous solution using alginate grafted polyacrylonitrile beads. Der Pharma Chem 2015;7(2):237–42.
[95] Daneshvar E, Vazirzadeh A, Niazi A, Kousha M, Naushad M, Bhatnagar A. Desorption of Methylene blue dye from brown macroalga: effects of operating parameters, isotherm study and kinetic modeling. J Clean Prod 2017;152:443–53. https://doi.org/10.1016/j.jclepro.2017.03.119.
[96] Eldin MS Mohy, et al. Carboxylated alginate hydrogel beads for methylene blue removal: formulation, kinetic and isothermal studies. Desalin Water Treat 2019;168:308–23. https://doi.org/10.5004/dwt.2019.24628.
[97] Marrakchi F, Khanday WA, Asif M, Hameed BH. Cross-linked chitosan/sepiolite composite for the adsorption of methylene blue and reactive orange 16. Int J Biol Macromol 2016;93:1231–9. https://doi.org/10.1016/j.ijbiomac.2016.09.069.
[98] Zeng L, et al. Chitosan/organic rectorite composite for the magnetic uptake of methylene blue and methyl orange. Carbohydr Polym 2015;123:89–98. https://doi.org/10.1016/j.carbpol.2015.01.021.
[99] Auta M, Hameed BH. Modified mesoporous clay adsorbent for adsorption isotherm and kinetics of methylene blue. Chem Eng J 2012;198–199:219–27. https://doi.org/10.1016/j.cej.2012.05.075.